Introduction

Total hip arthroplasty (THA) is one of the most successful procedures used to treat various hip disorders. Recent trends in a longer life expectancy of the population and an increased prevalence of THA in younger patients have led to an increase of the number of revision THAs. A major problem in a revision of a failed acetabular component is the loss of bone stock, which impairs implantation of new prosthetic components. The principles of acetabular reconstruction in revision THA are to restore pelvic bone stock, to create an acetabular bone bed for achieving stable fixation of the implants, and to rebuild an anatomical hip center with acceptable hip biomechanics and thereby to optimize joint stability.

Impaction bone grafting with morselized bone grafts is an attractive technique for restoring bone stock in acetabular reconstruction [1, 2]. This is a technically demanding option, and a wide variation in long-term outcomes has been reported [3–6]. Morselized bone chips are impacted layer by layer into the contained defects of the acetabulum with progressive forceful compaction in vivo using a metal impactor and slap hammer. This creates a neoacetabulum of an adequate new implant bed into which the acetabular component is implanted. The initial stability of the implant is essential for long-term survival, and it is likely that the initial stability of the acetabular component is determined mostly by compression resistance and interparticle shear resistance of the grafted layer, which can be affected by many parameters, including the initial stiffness and the size and quality of the bone chips [7–11]. In the standard technique of impaction bone grafting, the bone chips are impacted vigorously by a slap hammer to gain adequate stiffness of the graft aggregates, but intraoperative fractures of a thin-walled acetabular cortex are often encountered [6, 12]. Because there is no specific indicator for the intraoperative determination of when the graft has been compacted adequately, the surgeon may perform the procedure with undercompaction of the graft, resulting in instability and subsequent subsidence of the implant.

To avoid variability in clinical outcomes between surgeons, we developed a new technique of impaction bone grafting using an ex vivo compaction device. In this technique, sterilized washed morselized allograft bone chips are compacted ex vivo using the creep technique and the impaction technique to form various shapes of well-compacted, well-graded bone aggregates, which are then impacted into the contained cavity in vivo using the creep technique with impactors. In clinical practice, this technique offers good reproducibility when reconstructing the cavity and the segmental defects of the acetabulum. In this study, we introduce this new technique, and we describe the mechanical properties and three-dimensional (3D) micro-CT-based structural characteristics of the bone aggregates generated by this method to determine proper mechanical properties, osteoconductivity, and cement penetration of the bone aggregates for impaction bone grafting with morselized bone chips.

Materials and methods

Bone material

A whole femoral head was procured from a living donor at the time of primary THA for osteoarthritis. Donor selection, bone sterilization, and preservation were performed under the guidelines issued by the Japanese Society of Orthopedic Surgery. After removal of remnants of articular cartilage and synovial lining, donated bones are quarantined at −80°C for 6 months.

Graft preparation

Deep-frozen bone was sterilized by pasteurization using Lobator sd-2 (Telos, Marburg, Germany), and then ground into morselized bone chips in a bone mill (Japan Medical Materials, Osaka, Japan) once or twice to produce large- or small-sized particles, respectively (Fig. 1a). The size of the morselized particles was measured as described previously [13]: Large- and small-sized chips were 10.9 ± 1.9 and 3.69 ± 0.24 mm, respectively. Bone chips were placed into a sieve and washed using high-speed pulsatile lavage with normal saline solution to remove fat, marrow, and blood clots.

The ex vivo compaction device

The ex vivo compaction device was made of titanium alloy and stainless steel (Fig. 1b–d). This device was leverage equipped with a 50.6 cm lever. The stainless steel cylinder had an inner diameter of 46 mm, a height of 50 mm, and a wall thickness of 5.9 mm. The narrow gap (0.1 mm) between the base of the device and the cylindrical chamber allowed for fluid exudation. The inner molds were placed in the cylinder, the piston was placed on top, and compression force was then loaded with a stainless lever (Fig. 1d). Several shapes of the inner molds were provided to make a variety of shapes of the bone aggregates, including disc and lens shapes for medial wall defects of the acetabulum and thick talon shape for the peripheral wall defects (Fig. 1i).

Operating procedures

Impaction allograft reconstruction of the acetabulum using the ex vivo compaction device was performed on eight hips

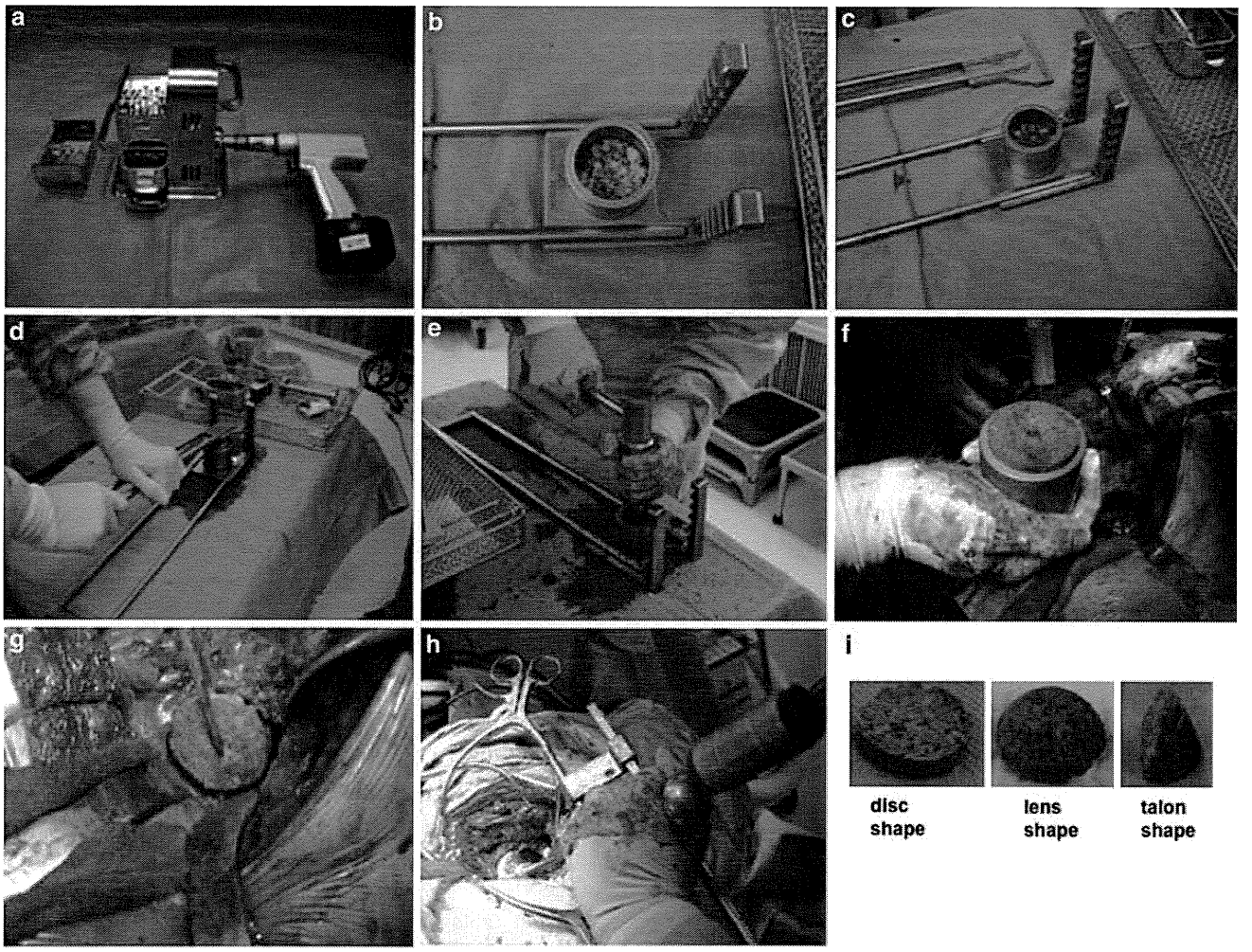

Fig. 1 Operating procedures of impaction bone grafting using the ex vivo compaction device in the acetabular reconstruction. **a** The bone mill used in this study. **b** Sterilized washed morselized allograft bone chips are placed in the chamber. **c** The patient's fresh blood is added. **d** Compression force is applied using the creep technique. **e** Impaction force is applied by the metal slap hammer. **f** The well-compacted, well-graded bone aggregate is formed. **g** The bone aggregate is grafted into the acetabulum. **h** The creep consolidation and additional light or moderate impaction form a good compacted layer within the acetabular defect. **i** Various shapes of bone aggregates can be produced

in eight patients (Table 1). All patients were female, and their average age was 63.5 years (range 48–74 years). The reasons for primary revision were aseptic loosening of the acetabular socket in five hips, migration of the bipolar outer head in two hips, and migration of the vitallium cup in one hip. Acetabular deficiencies were classified using the American Academy of Orthopaedic Surgeons (AAOS) classification [14]: type 2 in two hips and type 3 in six hips. Operations were performed through an anterolateral or posterolateral approach. After removal of the acetabular component, cement, and granulation tissues, the acetabular bone defect was assessed. The acetabular host bone was reamed until a bleeding bone bed was created or small drill holes were made for revascularization of the host bone. If necessary, segmental wall defects were contained with X-change metal mesh (Stryker Benoist Girard, Herouville-Saint-Clair, France) for peripheral wall defects and/or medial wall defects. To produce densely compacted bone aggregates for impaction bone grafting in acetabular reconstruction by an ex vivo compaction device, an adequate amount of bone chips was placed into the cylinder of the ex vivo compaction device, and 5 ml of fresh patient blood was fed into the stainless steel cylindrical chamber (Fig. 1b, c). Compaction was performed using the creep technique with a lever producing a constant compaction force for 90 s, and then a heavy impaction force was delivered five times with a metal slap hammer [15] (Fig. 1d, e). The compaction force reached a maximum of 3,300 N in the creep technique, and the heavy impaction by the hammer reached a maximum of 4,750 N (detailed data not shown). Various shapes of the bone aggregates were generated: lens or disc shaped for medial wall defects and

Table 1 Clinical cases

Case	Gender	Age (years)	AAOS classification	Cause of revision	Merle d'Aubigné and Postel score (pre-operation)	Merle d'Aubigné and Postel score (post-operation)	Follow-up period (months)
1	F	62	Type 3	Socket loosening	7	16	16
2	F	74	Type 3	Socket loosening	10	14	11
3	F	70	Type 3	Socket loosening	13	14	9
4	F	58	Type 3	Socket loosening	8	18	13
5	F	67	Type 2	Migration of bipolar outer head	10	16	13
6	F	65	Type 2	Migration of bipolar outer head	15	15	10
7	F	48	Type 3	Migration of vitallium cup	10	15	16
8	F	64	Type 3	Socket loosening	8	17	12

thick talon shaped for segmental defects under a metal mesh (Fig. 1i). The bone aggregates generated seemed dry and had enough stiffness to be held by a forceps (Fig. 1f, g). The bone aggregate was placed into the contained cavity with a constant compression force delivered using an impactor, and light or moderate impaction with a nylon hammer or a mallet (Fig. 1g, h). An X-Change metal mesh or an acetabular reconstruction plate (KT plate, Japan Medical Materials, Osaka, Japan) was used in all hips: a metal mesh for a segmental defect in three hips, for a medial wall defect in one hip, and a KT-plate in four hips in which a well-contained cavity was not obtained. A cross-linked ultra-high-molecular-weight polyethylene cup was cemented into the newly formed acetabular cavity. Before this operation, we obtained informed consent from the patients and their families.

Assessment of mechanical properties

The disc-shaped bone aggregates were produced by an ex vivo compaction device with 25 g of the indicated proportion of the mixture of large- and small-sized morselized bone chips: 25 g of large-sized bone chips in group 1, 16.7 g of large-sized and 8.3 g of small-sized bone chips in group 2, 8.3 g of large-sized and 16.7 g of small-sized bone chips in group 3, and 25 g of small-sized bone chips in group 4 ($n = 3$ for each group). The bone density of the bone aggregates comprising various sizes of 25 g of morselized bone chips was measured. Compression stiffness was measured by loading the bone aggregates in a uniaxial load-testing machine (Model 1123, Instron, Norwood, MA). The crosshead speed was 1 mm/min. The bone aggregates were compressed until 3,000 N without intervening stress relaxation. The load of 3,000 N is equivalent to the load applied to the hip joint when a person weighing 70 kg stands on one leg. The compression stiffness was calculated by the slope of the linear region in the compression stress–strain curve. The recoil was determined using the creep recovery of bone aggregates after unloading the compaction force, which represents a deformation rate relative to the initial thickness measured 90 s after ex vivo compaction.

Micro-CT-based structural analysis

Micro-CT-based structural analysis was performed based on our previous studies of porous biomaterials [16], and some modified algorithms were developed for this study. The void (pore) structure of the bone aggregates was assessed using a micro-CT system (SMX-100 CT SV3, Shimazu, Kyoto, Japan). The specimen in a cylinder made of acrylic resin was mounted on a rotatory stage and scanned in its entirety. Reconstructed images comprised 512 × 512 × 431 voxels, with a voxel size of 20 μm. These images were processed with a combination of free-ware (Image J, NIH, USA, http://rsb.info.nih.gov/ij/) and commercially available software (VG Studio MAX 2.0, Volume Graphics, Germany). The sequential analysis was conducted as follows. The image stacks were first read in as 3D slice series and subjected to image enhancement optimization by adjusting image contrast, brightness, and gamma value to highlight the contrast between the void area and the bone aggregates. Images were then smooth filtered (e.g., Gaussian filter) to reduce noise. The smoothed images then underwent a segmentation process using a 3D adaptive thresholding plugin for Image J (Adaptive 3D Threshold, C. Henden and J. Bache-Wiig, http://www.pvv.org/~perchrh/imagej/). This segmentation process converted each image to a binary image where the pixel population is assigned to either the foreground (bone) or the background (void).

For two-dimensional (2D) analysis, the binarized image stacks were subjected to 2D image processing to determine average pore size and pore size distribution. Using the watershed process in Image J, pores adjacent to each other were separated automatically, and pore area and perimeter

were measured quantitatively. The 2D pore size was calculated using the following equation:

$$PS_{2D} = \frac{4 \times PA}{PP},$$

where PS_{2D} is the 2D pore size, PA is the pore area, and PP is the pore perimeter. All pores in the image stacks were measured, and the pore size distributions were represented by a line histogram.

Image J and VG Studio MAX were used for 3D geometrical analysis. First, the binarized 3D image stacks were subjected to the Local Thickness plugin for Image J (RP. Dougherty and K–H. Kunzelmann, http://www.optinav.com/imagej.html). This plugin computed the local thickness of the 3D image stacks, defined as the diameter of the largest sphere that fits inside the pore and contains the point. The number of voxels with respective local thickness values was taken as the volume of pores with the corresponding diameter. Interconnected pores were defined as the pores that connected to the outer surface, and they were detected easily by tracing the interconnections. For the interconnectivity analysis, voxels with local thickness less than the respective values were set to foreground (blocking pore throats) [16]. The interconnected pore volume was then measured and regarded as the volume of the pore with a corresponding pore throat size. Cumulative volume fraction distribution was computed and then differentiated to give the pore size and pore throat size distributions.

Cement penetration

Ten grams of Simplex P bone cement (Stryker, Kalamazoo, MI, USA) with 0.25 ml of Indian black ink was prepared using a vacuum cement mixing system and applied to a bone aggregate in an acryl cylinder using an acetabular pressurizer (DePuy Orthopaedics, Inc., Warsaw, IN). After all the bone chips were removed, the maximal depth of cement penetration into the bone aggregates was measured ($n = 3$ for each group).

Statistical methods

In the compression test and the evaluation of cement penetration, three specimens were prepared for each composite condition of the bone aggregates, as shown in Figs. 3 and 5. The data in this study were analyzed using Dunnett's multiple comparison test. A p value <0.01 for the difference in values compared with those in group 1 was considered significant.

Institutional review board approval was obtained for publication of the study. The patients and their family were informed that data from the cases would be submitted for publication and gave their consent.

Results

Densely compacted bone aggregates were achieved in the acetabular reconstruction

The follow-up period of eight hips with impaction allograft reconstruction of the acetabulum using the ex vivo compaction device averaged 12.5 ± 2.6 months (range 9–16 months) (Table 1). The preoperative Merle d'Aubigné and Postel Score [17] of 10.1 ± 2.7 points improved to 15.6 ± 1.4 points postoperatively. No intraoperative complications occurred in any patient. Postoperative radiograms and CT showed densely packed allografts in the acetabular defect (Fig. 2). Neither migration nor loosening of the component was detected, indicating that initial stability of the component was sufficient in this procedure.

Compression stiffness of the bone aggregates did not differ significantly according to the size of bone chips

Bone density and mechanical properties of the bone aggregates made by an ex vivo compaction device were analyzed by in vitro experiments. First, the bone density of the bone aggregates comprising various sizes of 25 g of morselized bone chips was measured (Table 2). The bone density of each bone aggregate comprising various proportions of large- and small-sized bone chips ranged from 1.34 to 1.50 g/cm^3 and did not differ significantly between groups, although there was a slight correlation between the apparent density and size of the morselized bone chips. Next, the compression stiffness was measured by loading the bone aggregates in a uniaxial load-testing machine (Fig. 3a). The regression plot of stiffness versus strain showed that the mean final modulus of the bone aggregates was 13.5–15.4 MPa (Fig. 3b, c). The compression stiffness did not differ significantly between bone aggregates comprising only large-sized bone chips and those comprising small-sized bone chips, although there was slight correlation between compression stiffness and size of the morselized bone chips (Fig. 3c). The recoil was calculated in relation to the proportion of the large- and small-sized bone chips after the impaction force on the bone aggregate was released in the ex vivo compaction device. Interestingly, recoil occurred at 2.6–3.9% of the initial height of the aggregates, but did not differ significantly between the

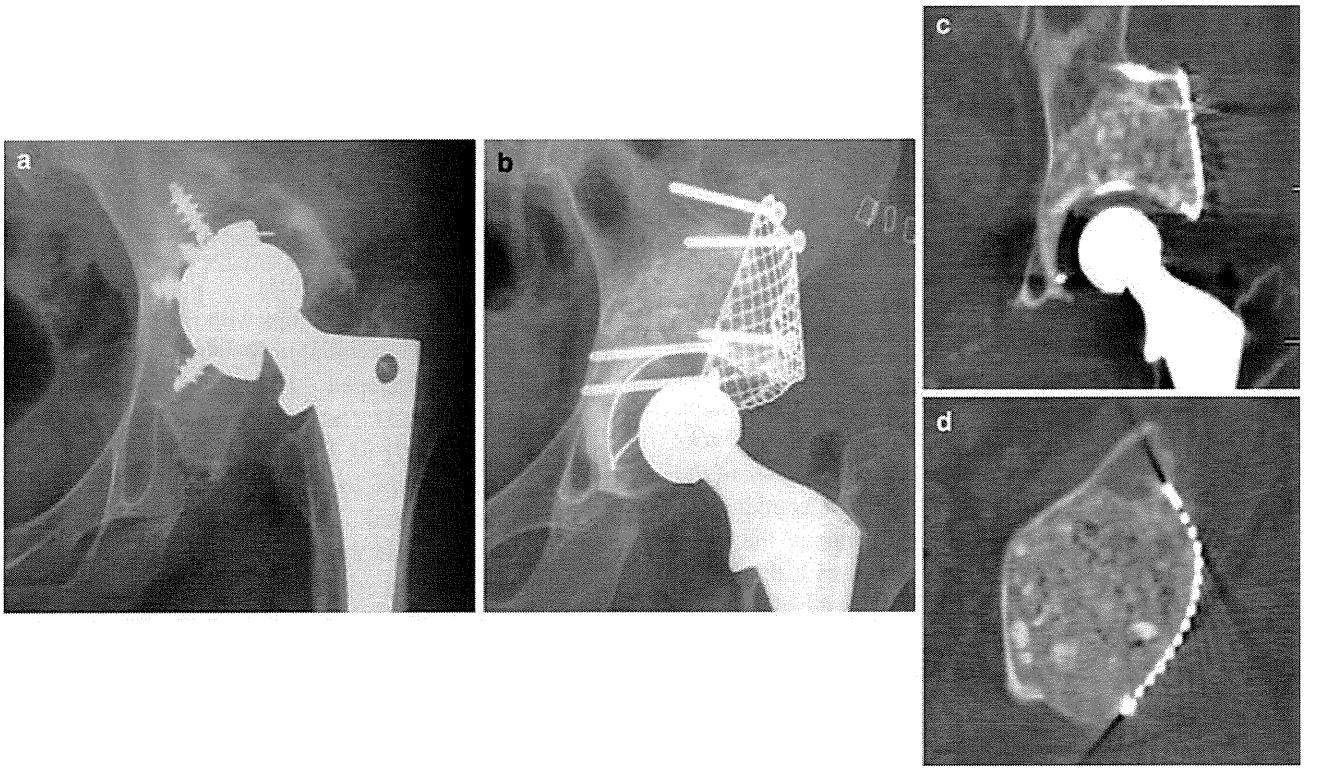

Fig. 2 Radiographs and CT images of the clinical cases. **a** Loosening of the acetabular component was revised using the impaction bone grafting technique. A postoperative radiograph **b** and CT images (**c**, **d**) show well-compacted bone grafting in an AAOS type 3 acetabular defect

Table 2 Bone density of the aggregates

Group	Ratio large size:small size	Mean ± SD (g/cm^3)	*p* value
1	All large-sized chips	1.34 ± 0.11	
2	2:1	1.48 ± 0.04	0.168
3	1:2	1.39 ± 0.03	0.677
4	All small-sized chips	1.50 ± 0.09	0.068

aggregates of different bone chip sizes (Fig. 3d). These results indicate that the ex vivo compaction device can produce well-compacted, well-graded bone aggregates with adequate mechanical stiffness from various sizes of the morselized bone chips.

The bone aggregates have a proper porous structure for osteoconduction

Two-dimensional pore size

Images of the microstructures of the bone aggregates obtained with micro-CT showed the composition of various sizes of morselized bone chips with a relatively heterogeneous distribution of pore sizes (Fig. 4a). The pore sizes of the bone aggregates were quantified from the image stacks, and the 2D pore size distributions are shown in Fig. 4b. The average pore size in the bone aggregates was 268–299 μm (Table 3), which is reported as the proper size for bone growth [18, 19].

Three-dimensional pore size

Further analysis of the void structure of the bone aggregates was performed three dimensionally (Fig. 4c, d), and it revealed that more than 95% of the pores in the bone aggregates possessed a throat diameter greater than 100 μm (Table 3), which is reported as desirable for tissue differentiation and osteoconduction [16]. Large pores with a diameter of more than 500 μm, which may be too large for bone growth [18, 19], tended to increase with the proportion of large-sized chips (Table 3). The mean porosity, pore size, pore throat size, volume fraction of pores with a narrow throat (less than 100 μm), and fraction of pores with a large diameter (more than 500 μm) were quantified from the micro-CT images and are shown in Table 3.

Bone aggregates made by large-sized bone chips exhibited better cement penetration

Cement penetration affects shear strength of the bone aggregates and the initial stability of the acetabular

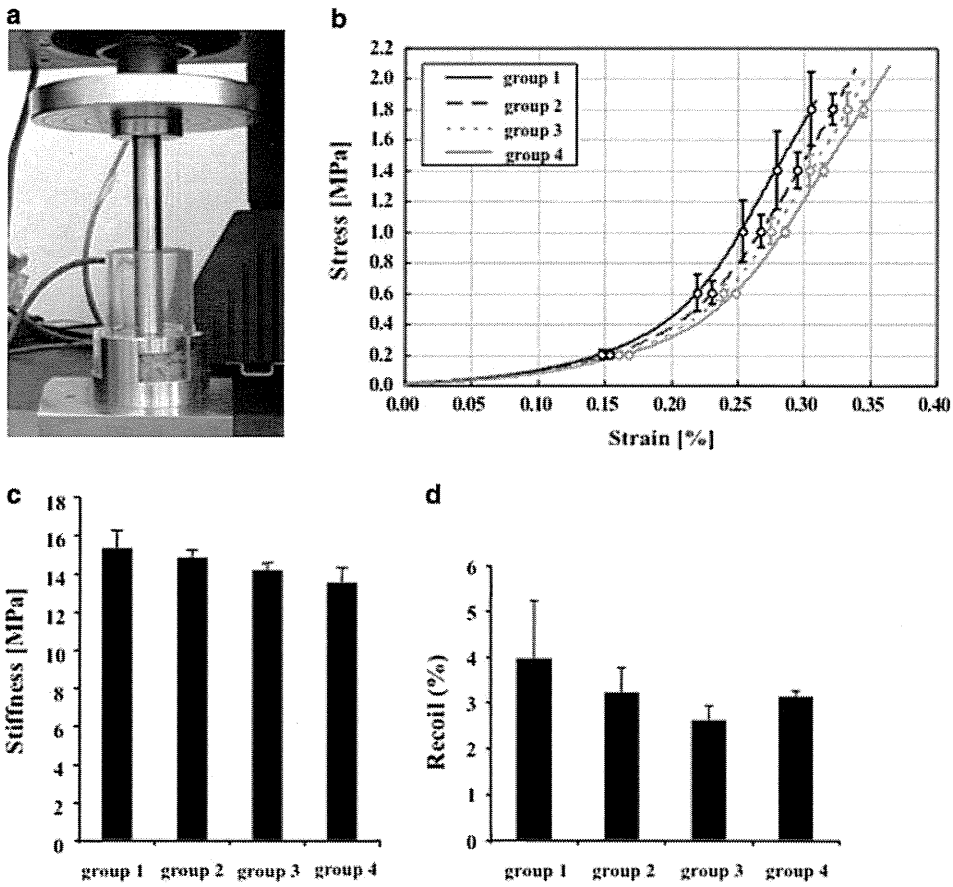

Fig. 3 Measurement of compression stiffness and recoil of the bone aggregates. **a** The force is measured with a load cell during constant displacement of the impactor gliding inside the cylinder containing the bone aggregate. **b** Compression stress versus strain curve for each specimen. **c** Compression stiffness is slightly but nonsignificantly higher in the bone aggregate containing only large-sized chips than in that containing small-sized chips. **d** Recoil of the bone aggregates does not differ significantly between the specimens

component [20]. The maximal depth of cement penetration depended on the size of the grafted bone chips (Fig. 5a, b). The average cement penetration depths were 0.76 ± 0.023 cm for the bone aggregates comprising only large-sized bone chips and 0.32 ± 0.056 cm for those comprising only small-sized bone chips.

Discussion

Impaction bone grafting in revision THA offers creation of a stable acetabular bone bed, secure prosthetic fixation, and restoration of bone stock. To gain successful clinical outcomes, bone graft preparation with morselized bone chips of various sizes is important for initial stability of the acetabular component and biological fixation of the component to the underlying host bone. However, this procedure is still technique-dependent, and there are no specific guidelines on how to produce well-compacted, well-graded bone aggregates having good mechanical and biological characteristics with various sized bone chips.

Mechanical properties of the bone aggregates

The initial stability of the acetabular component depends largely on the stiffness of the morselized allografts, which is related to the compression strength and the shear strength of the bone aggregates [7, 8, 11, 21, 22]. The principal concept of impaction bone grafting has been analyzed extensively, and it is likely that the mechanical characteristics of the bone aggregates obey the soil mechanics theory [23]. According to the Mohr-Coulomb failure criterion, the shear strength depends on the compression stress produced by the load, the angle of shearing resistance, and the interlocking of the bone particles. Thus, the impaction force has a substantial effect on the compression stiffness and shear strength of the graft aggregates. Morselized bone chips exhibit viscoelastic and viscoplastic behavior with partly recoverable and partly unrecoverable deformity under load [15]. Increasing the stiffness of the graft aggregates requires a maximal impaction force, which crushes the bone particles. However, administration of intermittent hard blows by a metal slap hammer in vivo dramatically increases the fracture risk of a thin medial

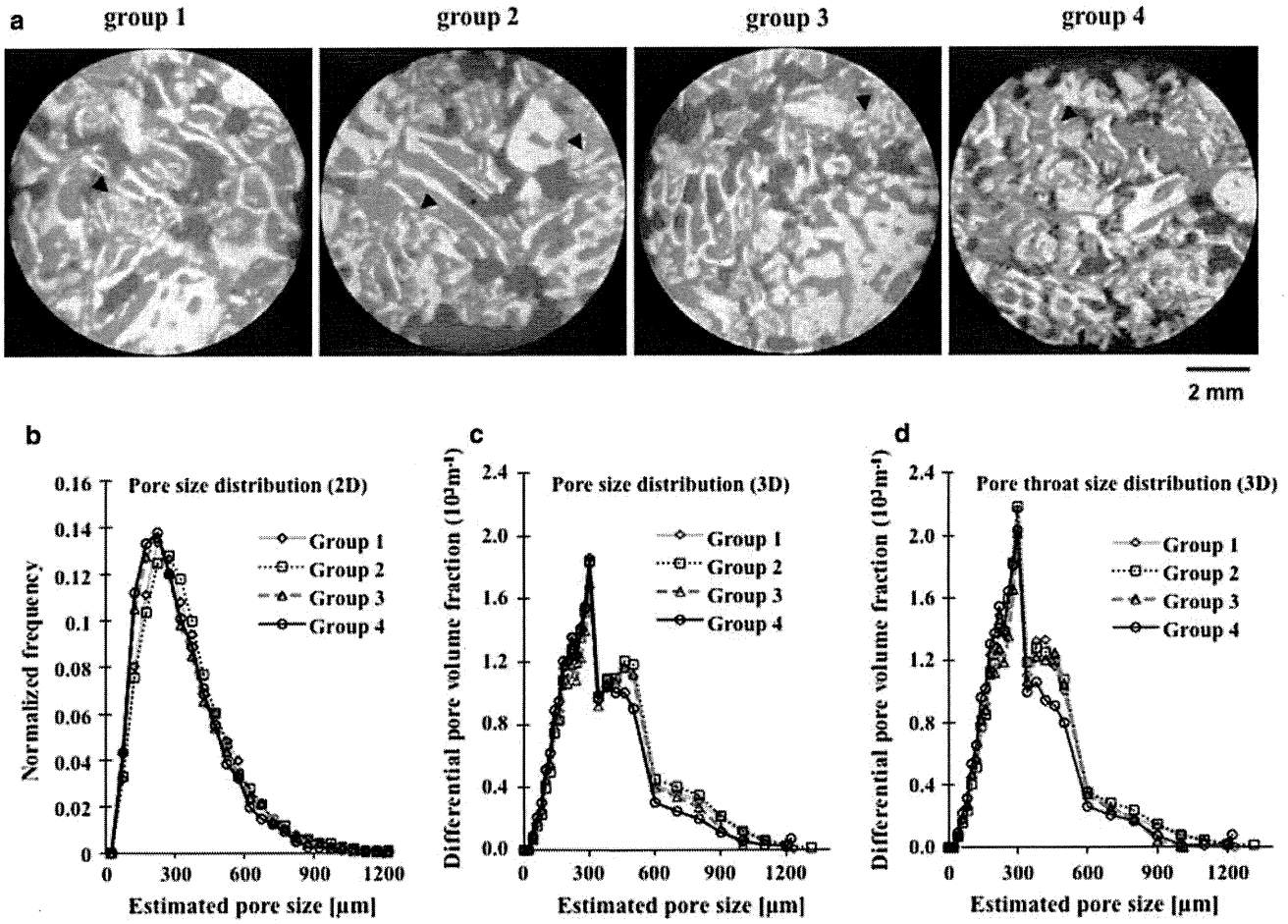

Fig. 4 Micro-CT-based structural analysis. **a** Micro-CT image of each specimen. *Arrowheads* denote crushed trabeculae. **b–d** Distribution of pore size based on **b** 2D analysis, **c** 3D analysis, and **d** pore throat size in each sample

Table 3 2D and 3D structural analysis of bone aggregates

Group	2D analysis	3D analysis				
	Pore size	Porosity (%)	Pore size[a]	Pore throat size[a]	Pore with narrow throat[b] (%)	Large pore[c] (%)
1	299 ± 191	63.1	393 ± 210	361 ± 186	2.7	26.4
2	299 ± 188	63.6	405 ± 211	372 ± 192	2.6	28.9
3	278 ± 183	57.4	376 ± 183	339 ± 146	3.4	23.8
4	268 ± 177	56.4	354 ± 191	328 ± 168	4.0	19.1

[a] Mean ± SD (μm)

[b] Volume fraction of pore with narrow throat (diameter less than 100 μm) in total pore

[c] Volume fraction of large pore (diameter more than 500 μm) in total pore

acetabular wall, and therefore a graft compaction method is required to yield greater strength and stiffness of the bone aggregates with increasing compaction force but with less risk of fracture. Albert et al. [15] reported that the creep technique, which involves holding a constant compaction force of 300 N for 90 s, improved the stiffness and shear strength by 14 and 16%, respectively, in vitro and suggested that the creep technique could provide a lower risk of intraoperative fracture over the use of larger impaction forces. However, they also showed that the higher impaction force increased stiffness and shear strength by 93 and 164%, respectively. On the basis of their data, a combination of the creep technique and the higher impaction force produced with a metal slap hammer may

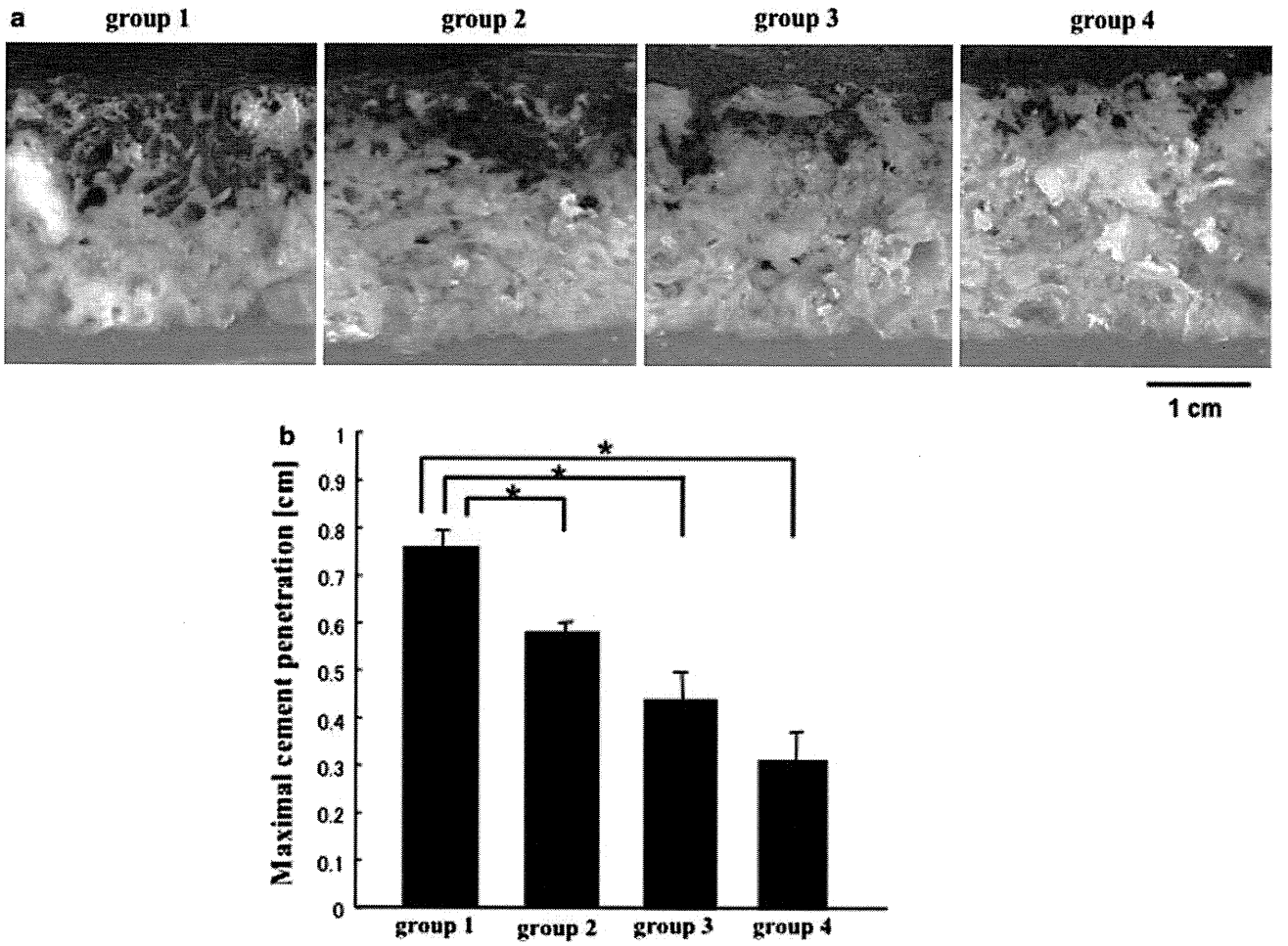

Fig. 5 Cement penetration into the bone aggregates. **a** Bone cement containing Indian black ink is applied to the bone aggregates with an acetabular pressurizer. **b** Maximal depth of cement penetration is increased in proportion to the amount of large-sized chips. *Asterisk* denotes significant difference $p < 0.01$

markedly improve the compression stiffness and shear strength of the bone aggregates. The ex vivo compaction device used in our study can hold a constant compaction force of more than 3,000 N and heavy load impaction force of more than 4,700 N. The compression stiffness of our postimpaction bone aggregates was 13.5–15.4 MPa, which is similar to the value reported in other studies [9, 24] and to that of cancellous bone from the femoral head as previously reported [25].

Bone density

The mechanical property of the bone aggregates also depends on the density of the packed bone chips and greater interparticulate surface area contact; increasing these variables produces more stiffness and less recoil of the bone aggregates [7, 11, 21]. To reduce the void space and to increase the interdigitation between bone particles, we removed fat, bone marrow, and blood clots by washing the morselized bone chips using high-speed pulsatile lavage. The patient's fresh blood was added to the sterilized washed morselized bone chips in the ex vivo compaction device because a small amount of fibrin formation decreases the recoil and increases the shear strength of the bone aggregates [26]. Importantly, slow compaction by the creep technique using the ex vivo compaction device allowed sufficient time for excess fluid exudation and deformation of the bone particles, and therefore produced dense and stiffer aggregates. The graft density of our bone aggregates was 1.34–1.50 g/cm^3, which is greater than that reported previously [27].

Size of the bone chips

The size of the bone chips also affects the stiffness of the bone aggregates. Bolder et al. [28] recommended larger sized chips for the acetabulum. They produced large bone chips (8–10 mm in diameter) by hand using a rongeur and

small bone chips (2 mm average diameter) using a bone mill. Radiometric analysis in a loading experiment revealed that the acetabular components had greater stability when large bone chips were used [20]. However, based on the Mohr-Coulomb failure criterion, both the angle of shearing resistance and the interlocking of the bone particles define the shear strength. Because the angle of shearing resistance depends on the distribution of particle size and because smaller particles fill the voids and interlock within the interparticulate spaces between larger particles, well-graded aggregates comprising a mixture of various-sized bone chips should have better mechanical characteristics compared with an ungraded mixture. Fosse et al. [8] reported that the bone aggregates with particles of uniform size have worse mechanical properties than those with a wider range of particle sizes. In our study, the mixture of different-sized bone chips did not markedly affect the stiffness properties of the bone aggregates. A possible reason for this difference relates to the different sizes of the bone particles. The bone mill used in our study cannot produce very small particles (less than 2 mm in diameter), and we used small-sized particles (3–4 mm in diameter) mixed with large-sized particles. Another possible explanation is that the ex vivo compaction device in our study loads more than 3,000 N of creep compression force and more than 4,700 N of impaction force, which crushes the trabecular structure of the bone chips. Small crushed bone fragments occupy the interparticulate spaces.

Recoil

In our study, recoil of the graft aggregates was 2.6–3.9% of the initial height of the compacted bone aggregates made by the ex vivo compaction device, and recoil did not correlate with the bone chip size. Previous studies showed that the impaction force, particle size, and fluid content influence recoil behavior significantly [11, 21]. Our ex vivo compaction device allows excess incompressible fluid exudation during use of the creep technique and crushes the trabecular structure of the bone particles during used of the creep and impaction technique, so that the particles lose their elasticity. In addition, small crushes of bone fragments and a mixture of various sizes of the bone chips reduce the void space and interlock each bone particle within the aggregates, reducing the recoil. Our micro-CT data visualized the collapsed trabeculae and the bone particles riding over each other.

Cement penetration

Closer packing increases the interparticulate contacts and the shear strength of the bone aggregates [7, 21]. However, well-compacted, well-graded bone aggregates can limit cement penetration into the interparticulate spaces. Because the bone cement creates a solid layer of bone at the graft-cement interface, greatly increasing the constant of the interlocking of the bone particles in the Mohr-Coulomb failure criterion contributes to the mechanical characteristics of the bone aggregates. Larger bone grafts should provide better penetration of the bone cement within the graft layer. Our data indicate that the maximal depth of cement penetration into the bone aggregates varies in relation to the proportion of large bone chips. This is because of the larger pores between the bone chips, even when a well-compacted bone aggregate can be produced using the ex vivo compaction device. Thus, bone aggregates made up with large-sized bone chips may produce better initial stability of the acetabular component.

Osteoconductivity

Several previous studies showed new bone formation onto the surfaces of the allograft bone chips and that regeneration and remodeling continue gradually for several years. Regeneration, remodeling, and a lasting bond between the graft and the host are prerequisites for the long-term success of impaction bone grafting. Pore size and interconnectivity are among the most important factors for osteoconduction by porous biomaterials [16, 18, 19, 29]. The optimal pore size for bone growth is generally considered to be 100–400 μm. We had some concerns that a well-compacted, well-graded mixture might hamper osteoconduction into the graft by filling up the interparticulate spaces. However, micro-CT analysis revealed that the grafts had adequate porous structure for osteoconduction and potential to encourage the bone graft healing process, which provides scaffolding for the ingrowth of vessels and osteoprogenitor cells to induce graft incorporation by the host [18, 19]. By contrast, bone aggregates comprising only large-sized bone chips tend to possess more pores, which may be too large to optimize bone growth, although few studies have reported on the adverse effects of large pores on osteoconduction [18, 19]. Thus, the bone aggregates produced with small-sized bone chips may provide superior osteoconductivity. Our data suggest that the graft layer on the host bone should comprise small-sized bone particles to facilitate bone ingrowth and that the layer on the implant side should be produced with large-sized bone particles to maximize cement penetration. Further studies are needed to confirm this hypothesis.

Clinical cases

In our clinical practice, we performed acetabular reconstruction by impaction bone grafting using the ex vivo compaction device in eight patients. Because most

migration and subsidence of the implant occurred during the first 3 months after implantation, as reported previously [30], the short-term outcome of the patients in this study indicated that the procedure was successful. We note that, after removing the compacted bone aggregates from the ex vivo compaction device, further creep consolidation of the bone aggregate with an impaction phantom formed a layer of well-compacted, well-graded bone aggregates in the acetabular defect in vivo. We also maintained the pressure on the graft bed to avoid possible recoil until the acetabular component was cemented. This procedure should contribute to the initial stiffness of the bone aggregates, leading to the initial stability of the acetabular component. We have applied this technique to acetabular reconstruction in patients, and no implant has exhibited any subsidence during a short-term follow-up period. Further clinical studies are required to determine the mid- and long-term outcomes of this technique.

In conclusion, the ex vivo compaction device produces well-compacted, well-graded allograft bone aggregates that possess adequate mechanical properties and putative osteoconductivity. Progressive compaction of layers of aggregates, comprising smaller sized chips at the host bone side and larger sized chips at the component side, may have the advantages of initial stability of the acetabular component and biological response of the grafted aggregates in acetabular reconstruction of revision THA.

Conflict of interest None of the authors of this manuscript has received any type of support, benefits, or funding from any commercial party related directly or indirectly to the subject of this article.

References

1. Gie GA, Linder L, Ling RS, Simon JP, Slooff TJ, Timperley AJ. Impacted cancellous allografts and cement for revision total hip arthroplasty. J Bone Joint Surg Br. 1993;75(1):14–21.
2. Slooff TJ, Huiskes R, van Horn J, Lemmens AJ. Bone grafting in total hip replacement for acetabular protrusion. Acta Orthop Scand. 1984;55(6):593–6.
3. Comba F, Buttaro M, Pusso R, Piccaluga F. Acetabular reconstruction with impacted bone allografts and cemented acetabular components: a 2- to 13-year follow-up study of 142 aseptic revisions. J Bone Joint Surg Br. 2006;88(7):865–9.
4. Iwase T, Masui T, Torii Y, Kouyama A. Impaction bone grafting for acetabular reconstruction: mean 5.5-year results in Japanese patients. Arch Orthop Trauma Surg 2009 (in press).
5. Schreurs BW, Bolder SB, Gardeniers JW, Verdonschot N, Slooff TJ, Veth RP. Acetabular revision with impacted morsellised cancellous bone grafting and a cemented cup. A 15- to 20-year follow-up. J Bone Joint Surg Br. 2004;86(4):492–7.
6. van Haaren EH, Heyligers IC, Alexander FG, Wuisman PI. High rate of failure of impaction grafting in large acetabular defects. J Bone Joint Surg Br. 2007;89(3):296–300.
7. Brewster NT, Gillespie WJ, Howie CR, Madabhushi SP, Usmani AS, Fairbairn DR. Mechanical considerations in impaction bone grafting. J Bone Joint Surg Br. 1999;81(1):118–24.
8. Fosse L, Ronningen H, Benum P, Lydersen S, Sandven RB. Factors affecting stiffness properties in impacted morsellized bone used in revision hip surgery: an experimental in vitro study. J Biomed Mater Res A. 2006;78(2):423–31.
9. Fosse L, Ronningen H, Lund-Larsen J, Benum P, Grande L. Impacted bone stiffness measured during construction of morsellised bone samples. J Biomech. 2004;37(11):1757–66.
10. Ornstein E, Franzen H, Johnsson R, Stefansdottir A, Sundberg M, Tagil M. Five-year follow-up of socket movements and loosening after revision with impacted morselized allograft bone and cement: a radiostereometric and radiographic analysis. J Arthroplasty. 2006;21(7):975–84.
11. Ullmark G, Nilsson O. Impacted corticocancellous allografts: recoil and strength. J Arthroplasty. 1999;14(8):1019–23.
12. Ornstein E, Atroshi I, Franzen H, Johnsson R, Sandquist P, Sundberg M. Early complications after one hundred and forty-four consecutive hip revisions with impacted morselized allograft bone and cement. J Bone Joint Surg Am. 2002;84-A(8):1323–8.
13. Tanabe Y, Wakui T, Kobayashi A, Ohashi H, Kadoya Y, Yamano Y. Determination of mechanical properties of impacted human morsellized cancellous allografts for revision joint arthroplasty. J Mater Sci Mater Med. 1999;10(12):755–60.
14. D'Antonio JA, Capello WN, Borden LS, Bargar WL, Bierbaum BF, Boettcher WG, Steinberg ME, Stulberg SD, Wedge JH. Classification and management of acetabular abnormalities in total hip arthroplasty. Clin Orthop Relat Res. 1989;243:126–37.
15. Albert C, Masri B, Duncan C, Oxland T, Fernlund G. Impaction allografting—the effect of impaction force and alternative compaction methods on the mechanical characteristics of the graft. J Biomed Mater Res B Appl Biomater. 2008;87(2):395–405.
16. Otsuki B, Takemoto M, Fujibayashi S, Neo M, Kokubo T, Nakamura T. Pore throat size and connectivity determine bone and tissue ingrowth into porous implants: three-dimensional micro-CT based structural analyses of porous bioactive titanium implants. Biomaterials. 2006;27(35):5892–900.
17. Merle d'Aubigné R, Postel M. Functional results of hip arthroplasty with acrylic prosthesis. J Bone Joint Surg Am. 1954;36:451–75.
18. Bobyn JD, Pilliar RM, Cameron HU, Weatherly GC. The optimum pore size for the fixation of porous-surfaced metal implants by the ingrowth of bone. Clin Orthop Relat Res. 1980;150:263–70.
19. Kujala S, Ryhanen J, Danilov A, Tuukkanen J. Effect of porosity on the osteointegration and bone ingrowth of a weight-bearing nickel-titanium bone graft substitute. Biomaterials. 2003;24(25):4691–7.
20. Arts JJ, Verdonschot N, Buma P, Schreurs BW. Larger bone graft size and washing of bone grafts prior to impaction enhances the initial stability of cemented cups: experiments using a synthetic acetabular model. Acta Orthop. 2006;77(2):227–33.
21. Dunlop DG, Brewster NT, Madabhushi SP, Usmani AS, Pankaj P, Howie CR. Techniques to improve the shear strength of impacted bone graft: the effect of particle size and washing of the graft. J Bone Joint Surg Am. 2003;85-A(4):639–46.
22. Voor MJ, White JE, Grieshaber JE, Malkani AL, Ullrich CR. Impacted morselized cancellous bone: mechanical effects of defatting and augmentation with fine hydroxyapatite particles. J Biomech. 2004;37(8):1233–9.
23. Craig RF. Craig's soil mechanics. 7th ed. New York: Spon Press; 2004.
24. Lunde KB, Kaehler N, Ronningen H, Fosse L. Pressure during compaction of morsellised bone gives an increase in stiffness: an in vitro study. J Biomech. 2008;41(1):231–4.
25. Ohman C, Baleani M, Perilli E, Dall'Ara E, Tassani S, Baruffaldi F, Viceconti M. Mechanical testing of cancellous bone from the femoral head: experimental errors due to off-axis measurements. J Biomech. 2007;40(11):2426–33.

26. Ahmed TA, Dare EV, Hincke M. Fibrin: a versatile scaffold for tissue engineering applications. Tissue Eng Part B Rev. 2008;14(2):199–215.
27. Bavadekar A, Cornu O, Godts B, Delloye C, Van Tomme J, Banse X. Stiffness and compactness of morselized grafts during impaction: an in vitro study with human femoral heads. Acta Orthop Scand. 2001;72(5):470–6.
28. Bolder SB, Schreurs BW, Verdonschot N, van Unen JM, Gardeniers JW, Slooff TJ. Particle size of bone graft and method of impaction affect initial stability of cemented cups: human cadaveric and synthetic pelvic specimen studies. Acta Orthop Scand. 2003;74(6):652–7.
29. Takemoto M, Fujibayashi S, Otsuki B, Matsushita T, Kokubo T, Nakamura T. 3-D anallysis of pore structure of porous biomaterials using micro focus X-ray computed tomography. Bioceramics. 2006;18:1095–8.
30. Ornstein E, Franzén H, Johnsson R, Sandquist P, Stefánsdóttir A, Sundberg M. Migration of the acetabular component after revision with impacted morselized allografts: a radiostereometric 2-year follow-up analysis of 21 cases. Acta Orthop Scand. 1999;70(4):338–42.

J Mater Sci: Mater Med (2011) 22:1803–1812
DOI 10.1007/s10856-011-4372-x

Nanostructured positively charged bioactive TiO_2 layer formed on Ti metal by NaOH, acid and heat treatments

Deepak K. Pattanayak · Seiji Yamaguchi · Tomiharu Matsushita · Tadashi Kokubo

Received: 15 April 2011 / Accepted: 4 June 2011 / Published online: 14 June 2011

Abstract Nanometer-scale roughness was generated on the surface of titanium (Ti) metal by NaOH treatment and remained after subsequent acid treatment with HCl, HNO_3 or H_2SO_4 solution, as long as the acid concentration was not high. It also remained after heat treatment. Sodium hydrogen titanate produced by NaOH treatment was transformed into hydrogen titanate after subsequent acid treatment as long as the acid concentration was not high. The hydrogen titanate was then transformed into titanium oxide (TiO_2) of anatase and rutile by heat treatment. Treated Ti metals exhibited high apatite-forming abilities in a simulated body fluid especially when the acid concentration was greater than 10 mM, irrespective of the type of acid solutions used. This high apatite-forming ability was maintained in humid environments for long periods. The high apatite-forming ability was attributed to the positive surface charge that formed on the TiO_2 layer and not to the surface roughness or a specific crystalline phase. This positively charged TiO_2 induced apatite formation by first selectively adsorbing negatively charged phosphate ions followed by positively charged calcium ions. Apatite formation is expected on the surfaces of such treated Ti metals after short periods, even in living systems. The bonding of metal to living bone is also expected to take place through this apatite layer.

D. K. Pattanayak (✉) · S. Yamaguchi · T. Matsushita · T. Kokubo
Department of Biomedical Sciences, College of Life and Health Sciences, Chubu University, 1200 Matsumoto-cho, Kasugai 487-8501, Japan
e-mail: deepak@isc.chubu.ac.jp; deepak_pattanayak@rediffmail.com

1 Introduction

Various surface treatment methods have been employed in an attempt to induce the bone-bonding property of titanium (Ti) metal and its alloys [1–14]. Of the treatment methods considered, the formation of sodium titanate on Ti metal by treating with both NaOH and heat has been shown to be effective for inducing apatite formation on Ti metal in the human body and causing Ti metal to bond to living bone through the apatite layer [15–18]. This method was applied to a porous Ti metal layer of an artificial hip joint, and the resulting bone bonding, i.e., a bioactive hip joint, has been clinically used in Japan since 2007 [19]. Apatite formation on NaOH- and heat-treated Ti metal in the living body was attributed to the negative surface charge of sodium titanate.

In contrast, it was recently shown that combining acid and heat treatment to form TiO_2 on Ti metal effectively induces apatite formation in the body environment and causes Ti metal to bond to living bone through the apatite layer [20]. The apatite formation in this case was attributed to the positive surface charge of TiO_2 [20].

Treatment with NaOH generates a bioactive surface with nanometer-scale roughness having a high specific surface area, but the sodium titanate formed by this treatment may have an undesirable effect on living cells in the narrow spaces of the porous material by the release Na^+ ions. In contrast, treatment with acid generates a bioactive surface with micrometer-scale roughness having a low specific surface area, but the TiO_2 formed by this treatment does not release ions that are liable to have adverse effects on living cells. Recently, it was shown that when Ti metal is subjected to HCl and heat treatment [21] subsequent to NaOH treatment, the bioactive TiO_2 layer that was formed had nanometer-scale roughness with a high specific surface area and releases no ions. In addition, porous Ti metal that

had been subjected to these treatments exhibited higher values of osteoconductivity and osteoinductivity than that subjected to simple NaOH and heat treatment [22–25].

In this study, we investigated the type of acid treatment that would be effective for inducing high apatite-forming ability of TiO_2 formed on Ti metal. Treatment with NaOH, acid, and heat were investigated. Factors governing their apatite-forming abilities were discussed in terms of their surface structure and properties.

Several articles that investigate the apatite-forming ability of TiO_2 that is formed on Ti metal by various treatment methods have been published [26–36]. However, the principal factors governing apatite formation on TiO_2 are not yet clearly understood.

2 Materials and methods

2.1 Preparation of the samples

Commercially pure Ti metal (Kobe Steel, Ltd, Japan) was cut into rectangular samples with dimensions of 10 × 10 × 1 mm^3, abraded with a #400 diamond plate, washed with acetone, 2-propanol, and ultra pure water for 30 min each in an ultrasonic cleaner, and then dried overnight in an oven at 40°C. Each sample was soaked in 5 ml of a 5 M NaOH solution at 60°C in an oil bath, shaken at 120 strokes/min for 24 h, and then gently washed with ultra pure water. Subsequently, the samples were soaked in 10 ml of an HCl, HNO_3, or H_2SO_4 solution with concentrations ranging from 0.5 to 100 mM at 40°C in an oil bath, shaken at 120 strokes/min for 24 h, and then gently washed with ultra pure water and dried overnight in an oven at 40°C. The samples were heated to 600°C at a rate of 5°C/min in an Fe–Cr electric furnace, maintained at this temperature for 1 h, and then cooled naturally to room temperature in the furnace.

2.2 Surface analysis of the treated Ti metal

The surface of the Ti metal treated as described above was analyzed using thin film X-ray diffraction (TF-XRD, RINT-2500, Rigaku Co., Japan). The X-ray source used was CuKα, and the angle of the incident beam was set to 1° against the sample surface. The same surface was coated with a Pt/Pd film and observed under a field emission scanning electron microscope (FE-SEM, Hitachi S-4300, Hitachi, Japan).

Ti metal plates with dimensions of 13 × 33 × 1 mm^3 were used to measure the zeta potential, and in the NaOH and acid treatments of the samples, the volumes of the NaOH and acid solutions used were increased to 20 and 30 ml, respectively. The treated Ti metal plates were electrically grounded to discharge any stray charges, and were immediately set in the zeta potential and particle size analyzer (ELS-Z1, Otsuka Electronics Co., Japan) using a glass cell for the plate sample. The zeta potential of the samples was measured under an applied voltage of 40 V in a 10 mM NaCl solution dispersing monitor particles of polystyrene latex particles (diameter = 500 nm) coated with hydroxyl propyl cellulose. Five samples were measured for each experimental condition, and the average value was used in our analysis.

2.3 Examination of the apatite-forming ability in a simulated body fluid (SBF)

The Ti metals treated as described above were soaked in 30 ml of an acellular SBF at 36.5°C with ion concentrations (Na^+ = 142.0, K^+ = 5.0, Mg^{2+} = 1.5, Ca^{2+} = 2.5, Cl^- = 147.8, HCO_3^- = 4.2, HPO_4^{2-} = 1.0, and SO_4^{2-} = 0.5 mM) nearly equal to those of human blood plasma. The SBF was prepared by dissolving reagent-grade NaCl, $NaHCO_3$, KCl, $K_2HPO_4{\cdot}3H_2O$, $MgCl_2{\cdot}6H_2O$, $CaCl_2$, and Na_2SO_4 (Nacalai Tesque Inc., Japan) in ultra pure water, and buffering at pH = 7.40 using tris (hydroxymethyl) aminomethane [$(CH_2OH)_3CNH_2$] and 1 M HCl (Nacalai Tesque Inc.) [37].

After soaking for periods of 1 min and 12 h, the samples were removed from the SBF, gently washed with ultra pure water for 5 min and dried at 40°C in an oven. The sample's surface was analyzed using X-ray photoelectron spectroscopy (XPS, ESCA-3300KM, Shimadzu Co., Japan) using MgKα radiation (λ = 9.8903 Å) as the X-ray source. The XPS take-off angle was set at 45°, which enabled the system to detect photoelectrons to a depth of 5–10 nm from the surface of the substrate. The binding energy of the measured spectra was calibrated by reference to the C_{1S} peak of the surfactant's CH_2 group on the substrate occurring at 284.6 eV.

After soaking in the SBF for 1 day, the surface was analyzed for apatite formation using TF-XRD and FE-SEM. To examine the stability of the apatite-forming ability in a humid environment, the NaOH, acid, and heat-treated samples were kept at a relative humidity of 95% at 80°C for 1 week, and the apatite formed on their surface in the SBF was examined using FE-SEM.

3 Results

3.1 Surface structure of the treated Ti metals

Figure 1 shows FE-SEM photographs of the surface of Ti metals subjected to various acid treatments after an NaOH treatment, compared with the surface of untreated Ti metal

and that treated with an NaOH solution. The treatments shown in Fig. 1 are designated according to the classifications shown in Table 1. A fine network structure of nanometer-scale was generated on the surface of the Ti metal by an initial NaOH treatment, and this remained essentially unchanged after a subsequent acid treatment, as long as the acid concentration was not high. The network structure was completely dissolved by treatment with a concentrated acid solution. The maximum concentration of the acid solution in which the fine network structure remained was 50 mM for the HCl and HNO_3 solutions, and 10 mM for the H_2SO_4 solution.

Figure 2 shows FE-SEM photographs of the surface of Ti metals subjected to a heat treatment after an NaOH and acid treatment. The surface structure formed on the Ti metals by the NaOH and acid treatments remained essentially unchanged after the heat treatment.

Figures 3 and 4 show the TF-XRD patterns of the surface of Ti metals subjected to NaOH and acid treatments, and those of Ti metals subjected to a subsequent heat treatment, respectively. From Fig. 3, it can be seen that a layer of sodium hydrogen titanate ($Na_xH_{2-x}Ti_3O_7$, $0 < x < 2$) had formed on the surface of Ti metal after the initial NaOH treatment [38], and that this was converted to

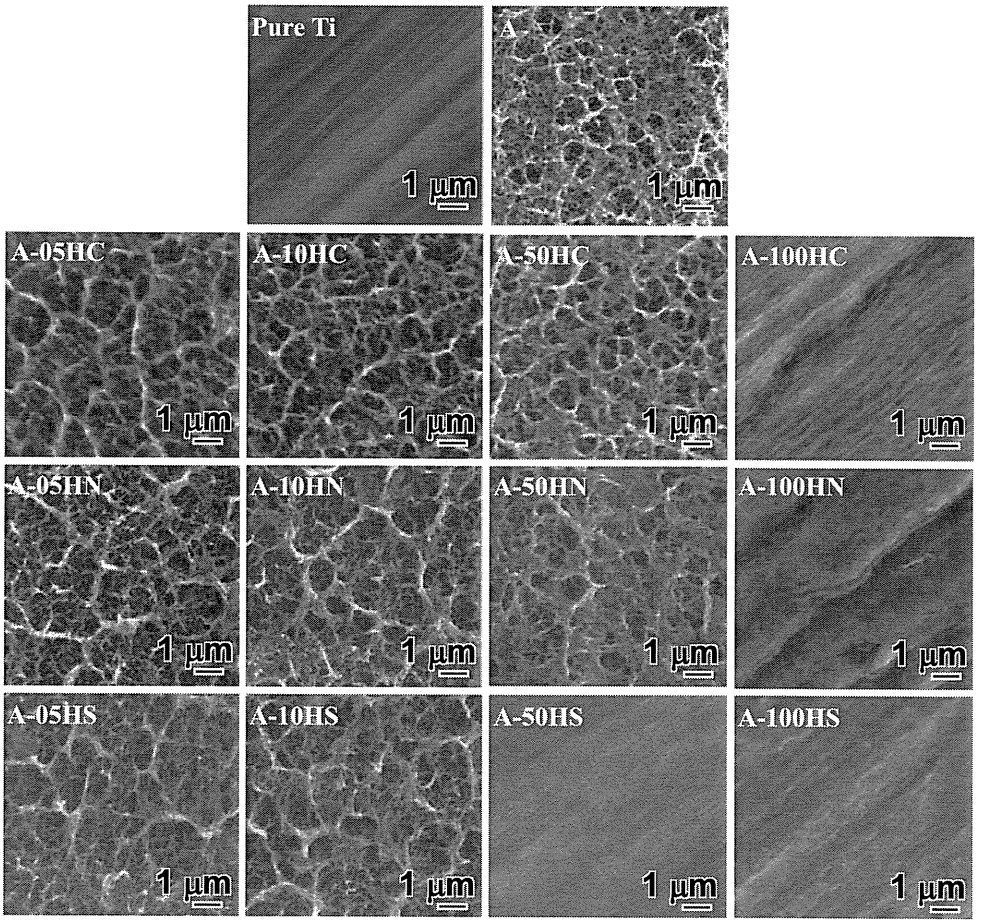

Fig. 1 FE-SEM photographs of surfaces of Ti metals subjected to various acid treatments after NaOH treatment, in comparison with those of Ti metal untreated and as-treated with NaOH. Explanation of notation is given in Table 1

Table 1 Notation of treatments

Notation	Treatments
A	Only NaOH treatment
A-05, 10, 50, or 100HC	A + 0.5, 10, 50 or 100 mM HCl treatments
A-05, 10, 50, or 100HC–H	A + 0.5, 10, 50 or 100 mM HCl + heat treatments
A-05, 10, 50, or 100HN	A + 0.5, 10, 50 or 100 mM HNO_3 treatments
A-05, 10, 50, or 100HN–H	A + 0.5, 10, 50 or 100 mM HNO_3 + heat treatments
A-05, 10, 50, or 100HS	A + 0.5, 10, 50 or 100 mM H_2SO_4 treatments
A-05, 10, 50, or 100HS–H	A + 0.5, 10, 50 or 100 mM H_2SO_4 + heat treatments

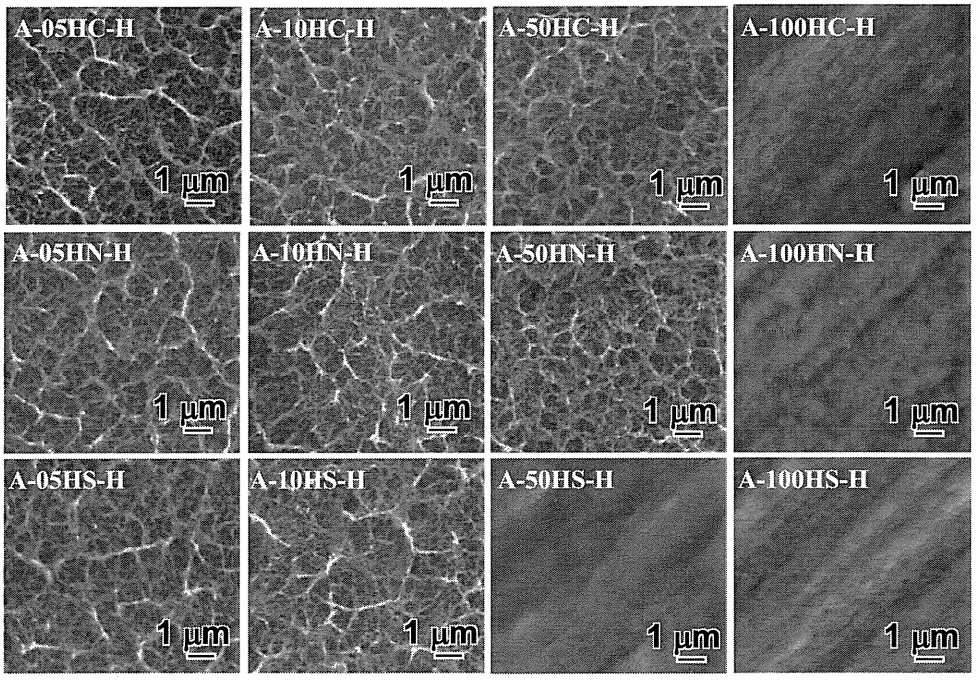

Fig. 2 FE-SEM photographs of surfaces of Ti metal subjected to the heat treatment after the acid and NaOH treatments, in comparison with those of Ti metal subjected to heat treatment without and after the NaOH treatment

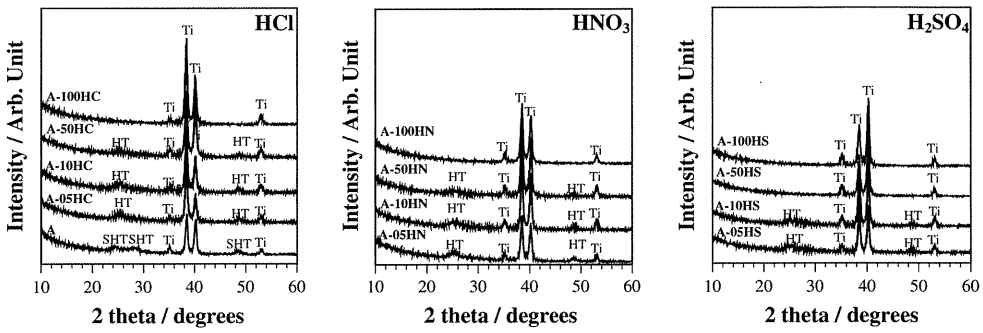

Fig. 3 TF-XRD of surfaces of Ti metal subjected to different chemical treatments. *Ti* α Ti, *HT* Hydrogen titanate, *SHT* Sodium hydrogen titanate

hydrogen titanate ($H_2Ti_3O_7$) [39] after a subsequent acid treatment, if the concentration of the acid solution was not high. After treatment with concentrated acid solutions, the sodium hydrogen titanate layer was completely dissolved. All the NaOH- and acid-treated Ti metals precipitated TiO_2 of anatase and/or rutile after the heat treatment (Fig. 4). The ratio of rutile to anatase increased with increasing concentration of the acid solution. Only the rutile phase was observed for the HCl and HNO_3 solutions with a concentration of 100 mM, and H_2SO_4 solutions with a concentration of 50 and 100 mM.

3.2 Apatite-forming ability of treated Ti metals in an SBF

Figures 5 and 6 show FE-SEM photographs of the surface of Ti metals soaked in an SBF for 1 day after different chemical treatments and a subsequent heat treatment, respectively. Spherical particles were observed on the surface, and these were identified as crystalline apatite from the TF-XRD data. Ti metals subjected to the chemical treatment alone did not form (or only formed a little) apatite on their surface in an SBF within a period of 1 day (Fig. 5). In contrast, all the Ti metals subjected to a heat treatment after a chemical treatment formed appreciable amounts of apatite on their surfaces in an SBF within 1 day (Fig. 6). The apatite-forming ability of the samples was high when the concentration of the acid solution used was greater than 10 mM.

Figure 7 shows FE-SEM photographs of the surface of Ti metals soaked in an SBF for 1 day after being kept at a relative humidity of 95% at 80°C for 1 week following NaOH, acid, and heat treatments. From Fig. 7, it can be seen that a high apatite-forming ability of such treated Ti metals was maintained, even in a humid environment.

3.3 Zeta potential of treated Ti metals

The zeta potentials of Ti metals treated with an acid solution after an NaOH treatment were not able to be

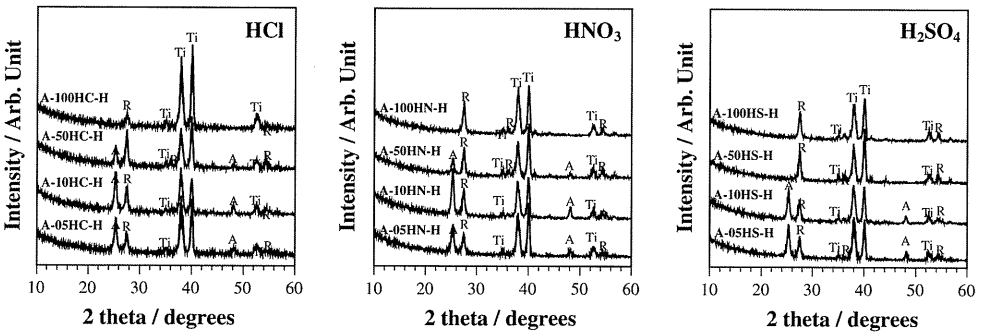

Fig. 4 TF-XRD of surfaces of Ti metal subjected to the heat treatment after different chemical treatments. *Ti* α Ti, *A* Anatase, *R* Rutile, *ST* Sodium titanate

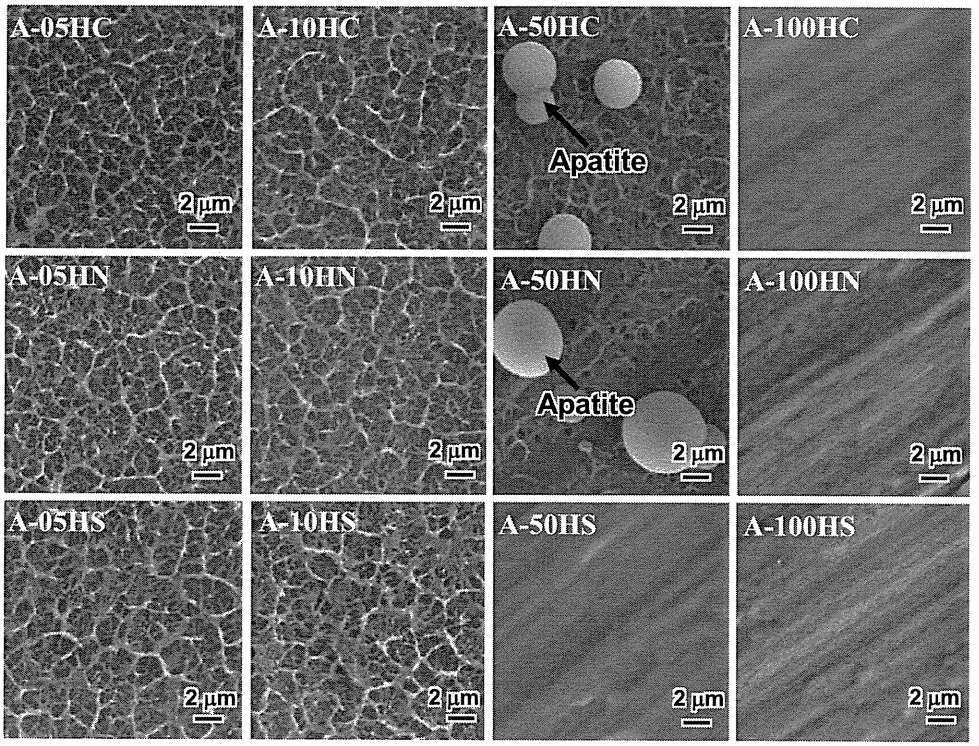

Fig. 5 FE-SEM photographs of surfaces of Ti metals soaked in SBF for 1 day after different chemical treatments

measured, as no insulating TiO_2 layer formed. This indicates that the zeta potential of these samples was almost zero. Figure 8 shows the zeta potentials of Ti metals subjected to a heat treatment after an NaOH and acid treatment. All the heat-treated samples showed a positive zeta potential, although the zeta potentials of Ti metals treated with 0.5 mM acid solutions were as low as 4 mV.

3.4 XPS spectra of treated Ti metals

Figure 9 shows the Ca_{2P} and P_{2P} XPS spectra of the surfaces of Ti metals soaked in an SBF for 1 min and 12 h after NaOH, acid, and heat treatments. From Fig. 9, it can be seen that all the treated Ti metals selectively adsorbed phosphate ions on their surface in an SBF within a period of 1 min, and later on, also adsorbed calcium ions to form calcium phosphate.

Figure 10 shows the Cl_{2P} and N_{1S} XPS spectra of the surfaces of Ti metal subjected to a heat treatment following an NaOH and 50 mM HCl or HNO_3 treatment. Also shown are the S_{2P} spectra of the surfaces of Ti metal treated with a 10 mM H_2SO_4 solution after an NaOH treatment after being subjected to a subsequent heat treatment and then kept at a relative humidity of 95% at 80°C for 1 week. From Fig. 10, it can be seen that chloride, nitrate, and sulfate ions were observed on the surface of Ti metals heat-treated after an HCl, HNO_3, and H_2SO_4 treatment following an NaOH treatment. Sulfate ions were detected on the surface of the samples before the heat treatment, and even after being kept in a humid environment for 1 week.

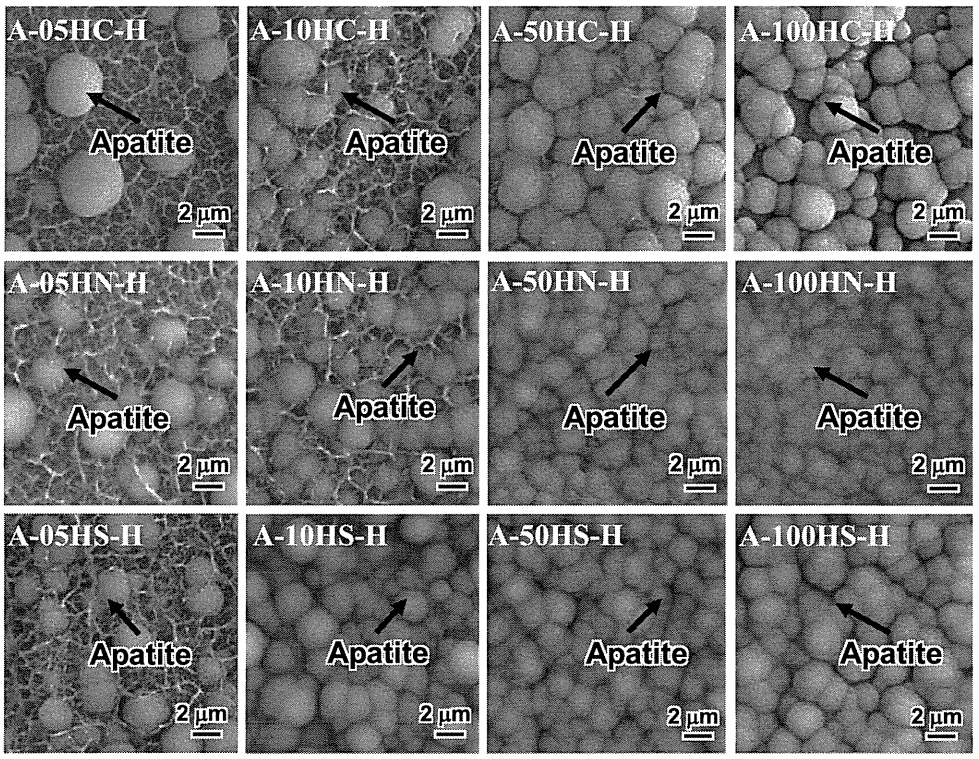

Fig. 6 FE-SEM photographs of surfaces of Ti metals soaked in SBF for 1 day after heat treatment following different chemical treatments

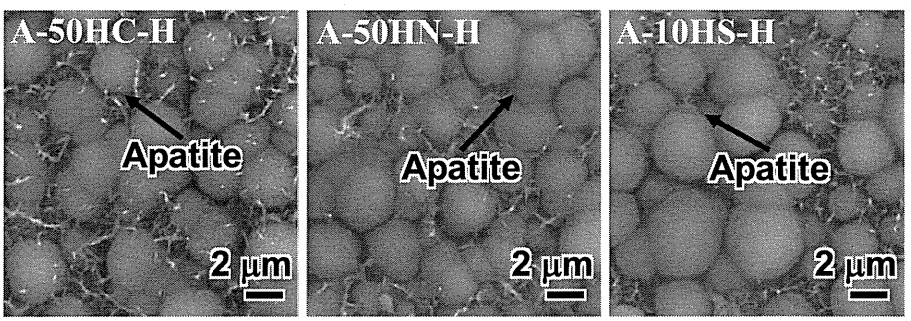

Fig. 7 FE-SEM photograph of surface of Ti metals soaked in SBF for 1 day, after kept in humid environment for 1 week following the NaOH, acid and heat treatments

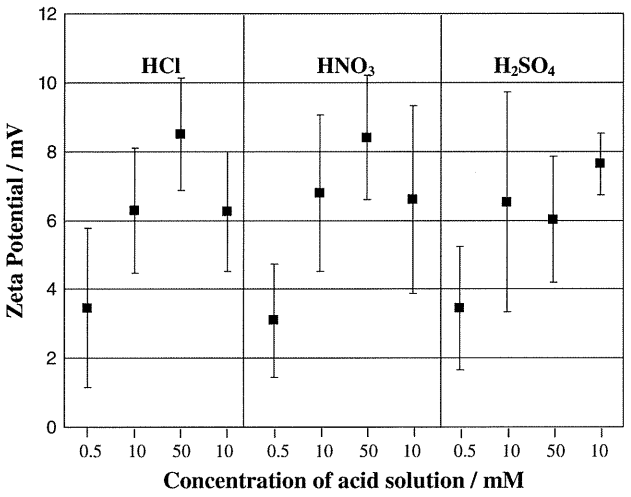

Fig. 8 Zeta potentials of surfaces of Ti metal plates after different chemical and heat treatments

4 Discussion

It is apparent from Figs. 1 and 2 that a nanometer-scale roughness is generated on the surface of Ti metals by an NaOH treatment and remained after the subsequent acid and heat treatments as long as the acid concentration is not high.

According to Figs. 3 and 4, sodium hydrogen titanate formed on Ti metals by an NaOH treatment is transformed into hydrogen titanate or completely dissolved by the subsequent acid treatment and then transformed into TiO_2 of anatase and/or rutile by the heat treatment.

It is apparent from Figs. 5 and 6 that the apatite-forming ability in an SBF of Ti metals subjected to an acid treatment after an NaOH treatment was very low before a heat treatment, but increased markedly after a heat treatment, irrespective of the type of acid solution used.

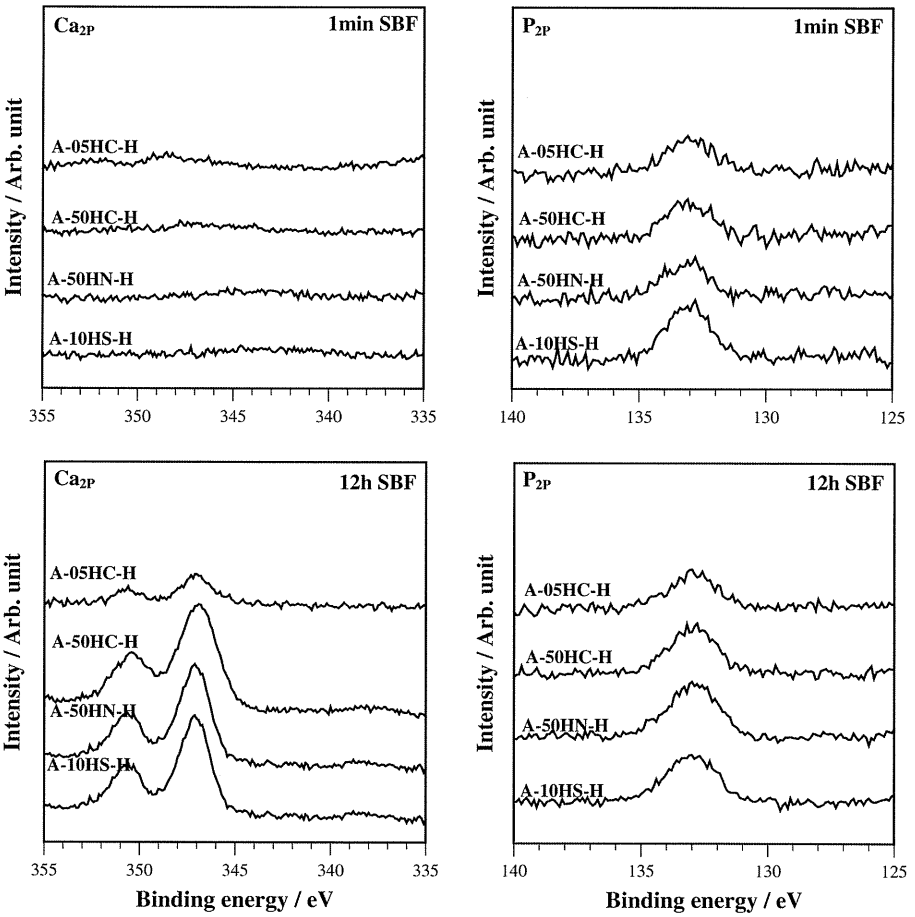

Fig. 9 XPS spectra of surfaces of Ti metals soaked in SBF for 1 min and 12 h after different chemical and heat treatments

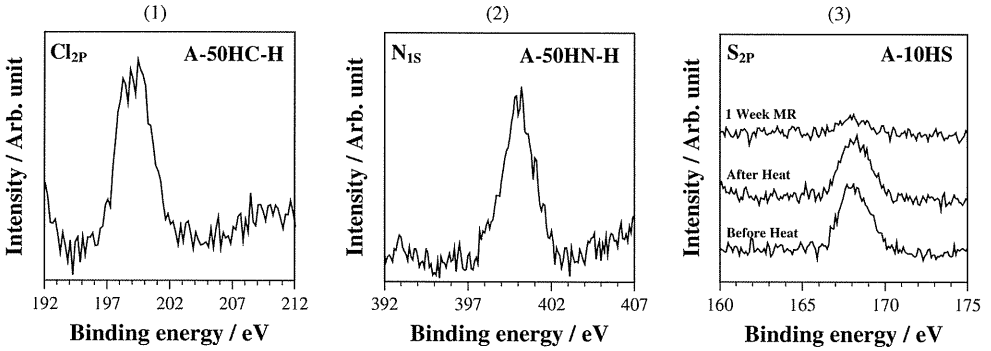

Fig. 10 XPS spectra of surfaces of Ti metals subjected to various chemical and heat treatments. *1* after heat treatment following NaOH and 50 mM HCl treatment; *2* after heat treatment following NaOH and 50 mM HNO_3 treatment; *3* before and after heat treatment following the NaOH and 10 mM H_2SO_4 treatment, and after subsequent storage in 95% relative humidity at 80°C for 1 week

As described above, the surface roughness of Ti metal subjected to an acid treatment after an NaOH treatment did not change after a heat treatment. Therefore, the increase in the apatite-forming ability after the heat treatment cannot be attributed to the change in surface roughness.

As described above, the surface phase of the Ti metals subjected to an acid treatment after an NaOH treatment was either hydrogen titanate or titanium before the heat treatment, while it was TiO_2 of anatase and/or rutile after the heat treatment. This indicates that TiO_2 is responsible for the high apatite-forming ability of the heat-treated Ti metal. However, apatite-forming ability of the heat-treated Ti metal does not depend upon the type of TiO_2 formed. For example, Ti metal treated with a 10 mM H_2SO_4 solution showed an almost equal apatite-forming ability to that of sample treated with a 100 mM H_2SO_4 solution (see

Fig. 6), although the former sample had a larger amount of anatase precipitated than rutile, whereas the latter sample had precipitated only rutile (see Fig. 4). Therefore, the apatite-forming ability of the heat-treated Ti metal samples cannot be attributed to the specific crystalline phase of TiO_2 precipitated.

The zeta potential of Ti metals subjected to an acid solution after an NaOH treatment was almost zero before a heat treatment, as described above. According to Fig. 8, the zeta potential of Ti metals subjected to an acid treatment after an NaOH treatment showed positive values after the heat treatment, and high values were observed when the concentration of the acid solution was greater than 10 mM, irrespective of the type of acid solution used. Figures 5 and 6 show that the apatite-forming ability of Ti metals subjected to an acid treatment after an NaOH treatment was increased by the heat treatment and became high when the concentration of the acid solution was greater than 10 mM, irrespective of the type of acid solution used.

When Ti metals have a positively charged surface, then negatively charged phosphate ions can be selectively adsorbed on their surface first. As these phosphate ions accumulate, the surface becomes negatively charged. As a result, positively charged calcium ions can be adsorbed on the surface to produce apatite. This sequential adsorption of phosphate and calcium ions was confirmed in the XPS spectra of Ti metals heat-treated after various acid treatments shown in Fig. 9. From these observations, it can be concluded that the high apatite-forming ability of the Ti metals heat-treated after an acid treatment following an NaOH treatment can be attributed to their positive surface charge.

The reason why the Ti metals heat-treated after an acid treatment following an NaOH treatment had a positive surface charge can be interpreted in terms of the acid groups adsorbed on their surface after the acid treatment. It was confirmed by the XPS spectra shown in Fig. 10 that sulfate ions were adsorbed on Ti metal soaked in an H_2SO_4 solution after an NaOH treatment, and that these remained on the Ti metal surface, even after subsequent heat treatment. Chloride ions and nitrate ions were also confirmed to be adsorbed on the Ti metal heat-treated after treatment in an HCl and HNO_3 solution, as shown in Fig. 10. These acid groups can dissociate from the surface of the Ti metals in an SBF to give an acidic surface environment. TiO_2 has been reported to be positively charged in acidic aqueous solutions, and its positive charge increases with decreasing pH of the solution [40, 41]. The acid solutions used in this study had pH values that decreased with increasing acid concentration, as shown in Table 2. All the acid solutions used in this study had pH values lower than 2 when their concentration was greater than 10 mM.

Table 2 pH values of acid solutions used in the present study

Solution	pH			
	0.5 mM	10 mM	50 mM	100 mM
HCl	3.46	2.13	1.47	1.16
HNO_3	3.50	2.14	1.46	1.15
H_2SO_4	3.10	1.98	1.25	1.05

The acid groups adsorbed on the Ti metals heat-treated after an acid treatment remained, even after the Ti metals were stored in a humid environment at high temperature, as shown in Fig. 10. Therefore, their high apatite-forming ability was maintained, even after storage in a humid environment at high temperature (see Fig. 7).

We have shown in a separate article that Ti metal heat-treated after H_2SO_4/HCl mixed acid treatment without being subjected to NaOH treatment formed TiO_2 layer [20] that formed apatite on its surface in a body environment and tightly bonded to living bone. The formation of apatite on the surface was also attributed to positive surface charge [20]. Our present results show that apatite formation induced by the positive surface charge of the Ti metal heat-treated after acid treatment is not specific to the use of a mixed acid solution, but is independent of the type of acid solution used, and is also independent of the surface condition before the acid treatment.

It has been shown previously that a porous Ti metal heat-treated after an HCl treatment following an NaOH treatment exhibits high osteoconductivity [22, 42] as well as osteoinductivity [23, 24]. This type of bioactive porous Ti metal is now being subjected to clinical trials for application in spinal fusion devices after animal experiment [25]. Our results provide a contribution to the development of porous Ti metals with higher osteoconductivity and osteoinductivity.

5 Conclusions

Nanometer-scale roughness was generated on the surface of Ti metal by NaOH treatment and remained even after formation of titanium oxide by the subsequent acid and heat treatments, as long as the acid concentration was not high. Ti metal treated with HCl, HNO_3 and H_2SO_4 solutions after an NaOH treatment showed high apatite-forming ability in an SBF after a subsequent heat treatment, especially when the acid concentration was greater than 10 mM. This was not attributed to either the surface roughness induced by the chemical treatment or to the specific crystalline phase precipitated on the Ti metal, but to the positive surface charge of the TiO_2 precipitated on the Ti metal by the acid and heat treatments. The positively

charged Ti metals first adsorbed the negatively charged phosphate ions in an SBF, and then the positively charged calcium ions to form apatite on their surface.

Such treated Ti metals are expected to form apatite on their surface in a short period, even in a living body, and can bond to living bone through this apatite layer. These findings will contribute to the development of porous Ti metal with higher osteoconductivity and osteoinductivity.

Acknowledgments The present authors acknowledge Prof. Y. Taga of Chubu University, Japan for his assistance in the XPS measurements. Useful suggestions by Dr. T. Kizuki and Prof. H. Takadama of Chubu University are also acknowledged.

References

1. Hanawa T, Kamimura Y, Yamamoto S, Kohgo T, Amemiya A, Ukai M, Murakami H, Asaoka K. Early bone formation around calcium-ion-implanted titanium inserted into rat tibia. J Biomed Mater Res. 1997;36:131–6.
2. Armitage DA, Mihoc R, Tate TJ, McPhail DS, Chater R, Hobkirk JA, Shinawi L, Jones FH. The oxidation of calcium implanted titanium in water: a depth profiling study. Appl Surf Sci. 2007; 253:4085–93.
3. Nayab SH, Jones FH, Olsen I. Effect of calcium ion implantation on bone cell function in vitro. J Biomed Mater Res. 2007;83A: 296–302.
4. Sul YT. The significance of the surface properties of oxidized titanium to the bone response: special emphasis on potential biochemical bonding of oxidized titanium implant. Biomaterials. 2003;24:3893–4007.
5. Song WH, Ryu HS, Hong SH. Apatite induction on Ca-containing titania formed by micro-arc oxidation. J Am Ceram Soc. 2005;88:2642–4.
6. Frojd V, Franke-Stenport V, Meirelles L, Wennerberg A. Increased bone contact to a calcium-incorporated oxidized commercially pure titanium implant: an in vivo study in rabbits. Int J Oral Maxillofac Surg. 2008;37:561–6.
7. Wu J, Liu ZM, Zhao XH, Gao Y, Hu J, Gao B. Improved biological performance of microarc-oxidized low-modulus Ti–24Nb–4Zr–7.9Sn alloy. J Biomed Mater Res. 2010;92B:298–306.
8. Whiteside P, Matykina E, Gough JE, Skeldon P, Thompson GE. In vitro evaluation of cell proliferation and collagen synthesis on titanium following plasma electrolytic oxidation. J Biomed Mater Res. 2010;94A:38–46.
9. Nakagawa M, Zhang L, Udoh K, Matsuya S, Ishikawa K. Effects of hydrothermal treatment with $CaCl_2$ solution on surface property and cell response of titanium implants. J Mater Sci. 2005;16:985–91.
10. Park JW, Park KB, Suh JY. Effects of calcium ion incorporation on bone healing of Ti6Al4V alloy implants in rabbit tibiae. Biomaterials. 2007;28:3306–13.
11. Ueda M, Ikeda M, Ogawa M. Chemical–hydrothermal combined surface modification of titanium for improvement of osteointegration. J Mater Sci Eng C. 2009;29:994–1000.
12. Chen XB, Li YC, Plessis JD, Hodgson PD, Wen C. Influence of calcium ion deposition on apatite-inducing ability of porous titanium for biomedical applications. Acta Biomater. 2009;5:1808–20.
13. Park JW, Kim YJ, Jang JH, Kwon TG, Bae YC, Suh JY. Effects of phosphoric acid treatment of titanium surfaces on surface properties, osteoblast response and removal of torque forces. Acta Biomater. 2010;6:1661–70.
14. Kokubo T, Miyaji F, Kim HM, Nakamura T. Spontaneous formation of bone-like apatite layer on chemically treated titanium metals. J Am Ceram Soc. 1996;79:1127–9.
15. Kim HM, Miyaji F, Kokubo T, Nakamura T. Preparation of bioactive Ti and its alloy via simple chemical surface treatment. J Biomed Mater Res. 1996;32:409–17.
16. Yan WQ, Nakamura T, Kobayashi M, Kim HM, Miyaji F, Kokubo T. Bonding of chemically treated titanium implants to bone. J Biomed Mater Res. 1997;37:267–75.
17. Yan WQ, Nakamura T, Kawanabe K, Nishiguchi S, Oka M, Kokubo T. Apatite layer-coated titanium for use as bone bonding implants. Biomaterials. 1997;18:1185–90.
18. Nishiguchi S, Fujibayashi S, Kim HM, Kokubo T, Nakamura T. Biology of alkali- and heat-treated titanium implants. J Biomed Mater Res. 2003;67A:26–35.
19. Kawanabe K, Ise K, Goto K, Akiyama H, Nakamura T, Kaneuji A, Sugimori T, Matsumoto T. A new cementless total hip arthoplasty with bioactive titanium porous-coating by alkaline and heat treatment: average 4.8-year results. J Biomed Mater Res. 2009;90B:476–81.
20. Kokubo T, Pattanayak DK, Yamaguchi S, Takadama H, Matsushita T, Kawai T, Takemoto M, Fujibayashi S, Nakamura T. Positively charged bioactive titanium metal prepared by simple chemical and heat treatments. J R Soc Interface. 2010;7:S503–13.
21. Pattanayak DK, Kawai T, Matsushita T, Takadama H, Nakamura T, Kokubo T. Effect of HCl concentrations on apatite-forming ability of NaOH–HCl– and heat-treated titanium metal. J Mater Sci: Mater Med. 2009;20:2401–11.
22. Fujibayashi S, Neo M, Kim HM, Kokubo T, Nakamura T. Osteoinduction of porous bioactive titanium metal. Biomaterials. 2004;25:443–50.
23. Takemoto M, Fujibayashi S, Neo M, Suzuki J, Kokubo T, Nakamura T. Mechanical properties and osteoconductivity of porous bioactive titanium. Biomaterials. 2005;26:6014–23.
24. Takemoto M, Fujibayashi S, Neo M, Suzuki J, Matsushita T, Kokubo T, Nakamura T. Osteoinductive porous titanium implants: effect of sodium removal by dilute HCl treatment. Biomaterials. 2006;27:2682–91.
25. Takemoto M, Fujibayashi S, Neo M, So K, Akiyama N, Matsushita T, Kokubo T, Nakamura T. A porous bioactive titanium implant for spinal inter body fusion: an experimental study using a canine model. J Neurosurg Spine. 2007;7:435–43.
26. Uchida M, Kim HM, Kokubo T, Fujibayashi S, Nakamura T. Effect of water treatment on the apatite-forming ability of NaOH-treated titanium metal. J Biomed Mater Res. 2002;63:522–30.
27. Wang XX, Hayakawa S, Tsuru K, Osaka A. Bioactive titania gel layers formed by chemical treatment of Ti substrate with a H_2O_2/HCl solution. Biomaterials. 2002;23:1353–7.
28. Wang XX, Yan W, Hayakawa S, Tsuru K, Osaka A. Apatite deposition on thermally and anodically oxidized titanium surfaces in a simulated body fluid. Biomaterials. 2003;24:4631–7.
29. Yang B, Uchida M, Kim HM, Zhang X, Kokubo T. Preparation of bioactive titanium metal via anodic oxidation treatment. Biomaterials. 2004;25:1003–10.
30. Rohanizadeh R, Al-Sadeq M, LeGeros RZ. Preparation of different forms of titanium oxide on titanium surface: effects on apatite deposition. J Biomed Mater Res. 2004;71A:343–52.
31. Wu JM, Hayakawa S, Tsuru K, Osaka A. Low-temperature preparation of anatase and rutile layers on titanium substrates and their ability to induce in vitro apatite deposition. J Am Ceram Soc. 2004;87:1635–42.
32. Lu X, Zhao Z, Leng Y. Biomimetic calcium phosphate coatings on nitric acid treated titanium surfaces. J Mater Sci Eng C. 2007;27:700–8.